Ettringite hysteresis under sorption from molecular simulations

Tulio Honorio, Maroua Maaroufi, Sirine Al Dandachli, Alexandra Bourdot

Version of Record: https://www.sciencedirect.com/science/article/pii/S0008884621002362
Manuscript_67139920bf229a12184944e1583bd2f6

Ettringite hysteresis under sorption from molecular simulations

Tulio Honorio[a,*], Maroua Maaroufi[a], Sirine Al Dandachli[a], Alexandra Bourdot[a]

[a]*Université Paris-Saclay, ENS Paris-Saclay, CNRS, LMT - Laboratoire de Mécanique et Technologie, 91190, Gif-sur-Yvette, France.*

Abstract

The response of ettringite under sorption is critical for the utilization of this mineral as an energy storage material and to understand the concrete durability problems associated with ettringite formation. We report molecular simulations directly sampling the osmotic ensemble to understand the sorption processes and structural changes in ettringite-metaettringite transition. Desorption branch and sorption-induced volume changes from simulations agree with the experiments. The structural changes at low relative humidity are analyzed, revealing for the first time details of metaettringite structure. The reversibility under sorption observed experimentally is captured by simulation in the ettringite domain. The reversibility in the conversion of metaettringite into ettringite is not captured by the direct simulations in the osmotic ensemble due to the large volume changes associated with ettringite desorption. Finally, we discuss the role of hydrogen bonds on the hysteresis in ettringite.

Keywords: Molecular dynamics; Grand Canonical Monte Carlo simulations; H-bonds; Hysteresis; Adsorption; Metaettringite.

* Corresponding author

Email address: tulio.honorio-de-faria@ens-paris-saclay.fr (Tullo Honorio)

Highlights

- Hybrid Grand Canonical Monte Carlo (GCMC) and Molecular Dynamics (MD) simulations are performed.
- Anisotropic large strain coefficient of crystal shrinkage of ettringite is provided.
- Entropy increases when ettringite converts into metaettringite.
- Sorption-induced stress may lead to columns collapse upon drying.
- H-bonds involving OH groups in columns play a role in hysteresis.

1. Introduction

Sorption processes play a critical role in ettringite volume stability, being fundamental to understand durability problems involving ettringite formation. The hysteresis under sorption is at the heart of the application of ettringite for thermal energy storage (TES) [1, 2]. The domain of performance of ettringite for TES, according to the relative humidity (RH) and temperature variations, has been under debate [3, 4]. At low RH, the formation of metaettringite, with a more disordered structure and lower water content, is reported [4]. The physical phenomena at the origins of volume stability and hysteresis, the reversibility of adsorption-desorption cycles in ettringite, and the structural changes associated with ettringite-metaettringite conversion are still poorly understood. The structure of metaettringite remains unknown to date [1]. Such critical information may constitute a milestone to understand the reversibility of the processes key in the utilization of ettringite for TES.

Atomistic simulation is a well-suited technique to provide atomic-level details of sorption processes microporous phases in cement-based materials at the time and length scales that are often difficult to probe experimentally and without the complexities related to the disorder and mixed phases that are often encountered in cement-based materials. Most of the existing studies on

molecular modelling of ettringite are in general related to its mechanical properties [5–10]. Interfacial properties of ettringite were studied using classical molecular dynamics [11] but at constant water content. Also, Medala et al. [12] investigate ettringite response under sorption and pH variations but using a primitive instead of a full atomistic approach. Atomic-level details are critical to understanding the structural changes undergone by ettringite at low RH leading to disorder. To the best of the authors' knowledge, no full atomistic simulations have yet been used to investigate the influence of relative humidity variations on ettringite behavior. These simulations can be used to understand, with atomic level detail, the hysteresis observed in drying-wetting in ettringite. Hysteresis is related to nonequilibrium phase behavior resulting from the existence of metastable states. This behavior should disappear in the equilibrium state, but often the equilibration time required might be very long in some microporous materials [13]. The nanoscale origins of hysteresis is still a topic under debate in the literature [13, 14].

In this work, we report full atomistic molecular simulations of ettringite under sorption. We deploy a hybrid simulation protocol combining molecular dynamics (MD) and grand canonical Monte Carlo (GCMC) techniques to sample the osmotic ensemble according to various imposed RH. With GCMC-MD simulations, the equilibrium water content and relaxed structures are obtained as a function of an imposed RH [15]. The empirical force field AFFF developed to molecular model of AF-phases in cement systems is deployed [9]. We simulate sorption isotherms and the associated volume changes and compare them against experimental data. We pay special attention to the structural changes at low RH, which is associated with metaettringite conversion. Our results shed light on the molecular mechanisms at the origin of hysteresis in ettringite.

2. Molecular models and methods

2.1. Atomic structure, force fields and sorption processes in ettringite / metaettringite

We adopt the hexagonal (P31c) atomic structure of ettringite resolved by Moore and Taylor [16]. Figure 1(A) shows a snapshot of ettringite structure at equilibrium at RH=100%. Ettringite possesses a structure in which zeolitic cavities left by $Ca_6Al_2(OH)_{12}$ columns (see Figure 1(B)) are occupied by water and sulfate ions. In the molecular formula of ettringite $Ca_6Al_2(SO_4)_3(OH)_{12}.nH_2O$ the water content is variable with $(n+6)$ = 30 - 33, where n stands for molecular water and the 6 for water that can be obtained from the 12 OH^- groups in the columns. We refer to this water content herein as being in the ettringite domain. Metaeetringite exhibits a lower water content with $(n+6)$ =11-13 [4].

Figure 1: (A) Snapshot of ettringite structure at equilibrium at RH=100% and (B) detail the columns of $Ca_6Al_2(OH)_{12}$. Atoms in the columns are colored as black spheres (the larger one refers to Al; the mean ones, to Ca; and the smaller ones to OH groups); Sulfates are colored as gray transparent particles. Boundary conditions and statistical ensembles of interest in the study of sorption of microporous adsorbing materials with significant sorption induced deformations: system at (C) constant swollen volume (μVT): desorption and adsorption occurs by emptying and filling, respectively, of the well defined zeolitic cavities by water molecules; (D) varying volume (responding to an imposed pressure: $N_s\mu$PT ensemble) so that the dimension may change due to crystal shrinkage in desorption or to accommodate new water molecules in adsorption; (E) constant unswollen volume (meta-ettringite domain, μVT): desorption and adsorption occurs by emptying and filling, respectively, of the space left in the disordered structures resulting from the collapse of columns.

A schematic representation of the boundary conditions of interest in the study of sorption of ettringite is proposed in Figure 1(C)-(E). Similar conditions have been proposed for other microporous adsorbing materials with significant sorption-induced deformations [17]. In the conversion ettringite-metaettringite the following situations are considered: (C) constant swollen volume: desorption and adsorption occurs by emptying and filling, respectively, of the well defined zeolitic cavities by water molecules; (D) varying volume (responding to an imposed pressure) so that the dimension may change due to crystal shrinkage in desorption or to accommodate new water molecules in adsorption; (E) constant unswollen volume (meta-ettringite domain): desorption and adsorption occurs by emptying and filling, respectively, of the space left in the disordered structures resulting from the collapse of columns.

Atoms interactions are modeled using the empirical force field AFFF [9] developed for molecular simulation of AF-phases in cement systems. AFFF captures reproduce the structural features and elastic response of ettringite and monosulfoaluminate as discussed in ref. [9]. The parameters of AFFF are described in the Supplementary Material.

2.2. Simulations in the osmotic and grand canonical ensembles

We aim at sampling the grand isobaric or osmotic ensemble ($N_s \mu PT$) in which the chemical potential μ(RH) of the water, the pressure P, and temperature T are imposed in a system with a constant number N_s of non-sorbent particles (the columns and sulfate ions, for ettringite), which gives the extensive measure required to quantify the system size [21]. The osmotic ensemble corresponds to a system that (i) may exchange energy and water molecules with an infinite reservoir imposing the temperature and the water chemical potential (or partial

pressure), and (ii) may exchange volume (or deformation) with the infinite reservoir which set the mechanical stress $\sigma = -P\mathbb{I}$, where $\mathbb{I}$ is the 3x3 identity matrix.

Hybrid GCMC-NPT simulations are carried out to sample the $N_s\mu PT$ ensemble. During the GCMC stage, water molecules are allowed to exchange with an infinite water reservoir at imposed chemical potential and temperature. For ambient temperatures, one may assume an ideal gas behavior for water since the temperature remains well below the critical point for water [14]. The chemical potential of water is computed from the relative humidity to be imposed by $\mu - \mu_0 \approx k_B T ln(RH) = k_B T ln(P/P_0)$, where k_B is the Boltzmann constant, P is the thermodynamic pressure in the system and P_0 is the saturated vapor pressure of pure water at a given temperature.

The dependence of P_0 on the temperature is accounted for using Clausius-Clapeyron relation [22]:

$$ln\left(\frac{P}{P_0}\right) = \frac{\Delta_{vap}H^{app}}{R}\left(\frac{1}{T_0} - \frac{1}{T}\right) \quad (1)$$

where $\frac{\Delta_{vap}H^{app}}{R}$ is the apparent enthalpy of vaporization (R being the gas constant and $\Delta_{vap}H^{app}$ =44.2 kJ/mol for SPC/E water [22]). For SPC/E water [22]. We obtain: $P_0(T = 291K) = 588$ Pa and $P_0(T = 298K) = 902$ Pa (for further comparison, we obtain $P_0(T = 300K) = 1017$ Pa, which is in exact agreement with NIST benchmark for SPC/E water [23]. SPC/E model underestimates the saturation pressure compared to experimental data for water).

A stress σ in the molecular dynamics NPT stage, and the six components of the (symmetric) stress tensor are controlled independently. Note that due to the column-like morphology of ettringite, the strategy of GCMC-NVT simulations having the basal spacing as

reaction coordinate (as generally adopted in investigations of layered materials [24, 25]) cannot be adopted here.

LAMMPS [26] is used in the simulations. A cutoff of 10Å is used for non-bond pair interactions. Tails corrections are used for Lennard-Jones potential. Ewald sum method is deployed to cope with long-range electrostatics. Time integration is performed using a 0.5 fs timestep. Nosé-Hoover thermostat and barostat are adopted with 100 and 1000 timesteps, respectively, as damping parameters. SHAKE algorithm [27] is used to constraint water molecules. In the GCMC stage, inserted atoms' temperature is rescaled ("tfac" of 6/3) to account for the rotational degrees of freedom of water. In the hybrid MD-GCMC protocol, each 1000 MD steps, 2000 Monte Carlo (MC) steps are performed (each Monte Carlo step being defined as one attempt to perform one unbiased insertion or suppression of a water molecules). Note that the variability in the water content observed in the production runs attest that even in crowded system insertion and suppression moves were working. The number of MC steps per MD-GCMC stage is more than 10-fold the number of water molecules present in the simulated systems at 100 % RH.

Hybrid GCMC-NVT (sampling the grand canonical ensemble) simulations are also performed in some cases for comparison (cases (C) and (E) in Figure 1).

To simulate desorption isotherms, we use as initial configuration the equilibrium configuration obtained for RH = 100 % at the T (=291 or 298 K) considered. At least 10 cycles of one million MC steps (a cycle of one million MC steps includes two-million MD steps in the hybrid MD-GCMC protocol) are performed for equilibration at the imposed RH. This number of cycles is enough for the system to reach equilibrium with stable internal energy and water content in the desorption branch. For results production and averaging, at least 10 cycles of one million MC steps are used.

To simulate the adsorption branch, we use as initial configuration the equilibrium configuration (i.e one of the equilibrium configurations obtained in the simulation for the desorption branch) obtained for various RH in both ettringite and metaettringite domains. To illustrate, one complete sorption cycle (the one in Figure 2 (B)) involves simulation in the desorption branch from 100 to 30 % RH, and then simulations for the adsorption branch in which the configuration obtained for 30% RH in the desorption branch is used as the initial configuration. Sorption cycles with rewetting at lower RH (1 and 0.1%RH) are also tested and discussed in the next section.

3. Results and Discussion

3.1. Sorption Isotherms

We compare the sorption isotherms obtained from simulations with the experimental data of Skoblinskaya et al. [28] (Figure 2) at T= 291 K, and Baquerizo et al. [3] (Figure 3.1) at T= 298 K. In both cases, the desorption branch obtained by simulations is in agreement with the experimental data. Simulation results of desorption can be fitted by a Langmuir isotherm (e.g. [17]):

$$n_{iso}(RH) = \frac{n_0 BP}{1 + BP} \qquad (2)$$

where the water partial pressure $P = RH.P_0$ is computed from the relative humidity and saturated vapor pressure of pure water P_0; n_0 denotes the sorption capacity; the parameter B corresponds to the slope of the adsorption isotherm at very low vapor pressures (i.e. when $P / P_0 \approx RH$). For both desorption simulations, we obtain by fitting $B = 0.9\ \mathrm{Pa}^{-1}$ and $n_0 = 32$ (= $(n + 6)$ per Ca_6Al_2).

Note that some of the 5 experiments performed by (Figure 2) show an increase in water content at high RH (R<h $> 80\%$). This increase is not observed in Baquerizo et al. [3] experiments and may be attributed to surface adsorption or capillary condensation. Microporous materials generally display Type I isotherms, i.e. the sorption isotherm is concave for entire range of the RH from 0 to 100% ($\frac{d^2 n_{iso}}{dP^2} < 0 \quad \forall P \in [0, P_0]$) as the one given by Langmuir isotherm (e.g. [17]).

The adsorption branches are shown in Figure 2(B)-(D) for Skoblinskaya et al. [28] data according to three different rewetting RH. For comparison, in the simulation we have considered the following rewetting RH: (B) 30%, (C) 1%, and (D) 0.1%. For the cycles with rewetting from RH of 30 and 1%, close loop reversible hysteresis is observed by both experiments and simulations. For the cycle with rewetting from 0.1% RH, the reversibility of the adsorption branch at high RH ($> 60\%$) is not captured by the simulations.

For comparison with Baquerizo et al. [3] (in Figure 3) adsorption results, we adopted a rewetting RH of 0.1% instead of RH = 0%. This choice was made because the water is quickly depleted in RH = 0% desorption simulation, leading to abrupt volume changes that may not occur in gradual drying of ettringite. Water depletion and volume changes in the RH = 0.1% desorption simulation are gradual allowing to follow with more details the structural changes related to the coupled sorption-induced deformations. The reversibility of the adsorption branch at high RH ($> 60\%$) is again not captured by the simulations.

Figure 2: Sorption isotherms obtained from simulation compared against Skoblinskaya et al. [28] experimental data (T = 291 K). The simulations were performed in the osmotic ensemble ($N_s \mu PT$). (A) Desorption branch compared to the experimental sets “A”-”E” as labeled in[28]. (B) and (C) Sorption cycles with close loop reversible hysteresis from 30 and 1 % RH (dark yellow labels),

respectively. (D) Sorption cycle with open-loop hysteresis: simulation cannot capture the reversibility under adsorption. We fit the simulated desorption and adsorption branches with Langmuir isotherms (Eq. 2). The standard deviations of water contents obtained from simulations are on the order of the symbol size and are not shown for conciseness.

Figure 3: Sorption isotherms obtained from simulation compared against Baquerizo et al. [3] experimental data (T = 298 K). We fit the simulated desorption and adsorption branches obtained in the osmotic ensemble with Langmuir isotherms (Eq. 2). Simulations in the osmotic ensemble (dark blue symbols, condition (D) in Figure 1) and in the grand canonical ensemble (yellow symbols, condition (C) and (E) in Figure 1) are shown. The standard deviations of water contents obtained from simulations are on the order of the symbol size and are not shown for conciseness.

Simulation in the grand canonical ensemble corresponding to the conditions (C) and (E) in Figure 1 are also plotted in Figure 3). The systems in the osmotic equilibrium follow a path that is similar to the swollen system in the grand canonical ensemble in the desorption branch and the unswollen system in the grand canonical ensemble in the adsorption branch. The transition of the unswollen state can be attributed to the sorption-induced stress, also observed in other microporous materials [29], exerted in the columns. This stress is anisotropic (with more negative pressure being obverded along x and y direction) and on the order of hundreds of MPa at low RH as shown in Figure 4). Sorption-induced stress becomes significantly negative promoting columns collapse a reduction in the free volume in ettringite at RH below 10%.

Figure 4: Sorption-induced stress computed in grand canonical simulation in swollen state

(condition Figure 1(C)) as a function of the RH: component of pressure tensor according to x, y and z directions.

Desorption in ettringite is associated with large changes in lattice parameters and volume, shown in Figure 5(A)-(D) comparing simulation results with the experimental data of Baquerizo et al. [3], Zhou et al. [4] and Gard (as cited by [4]). The volume changes observed in simulations are consistent with the experimental evidence. We fit each lattice parameter x (=a,b or c) obtained from the simulations with the expression:

$$x(RH) = \frac{\delta_0 BP_0 RH}{1 + BP_0 RH} + x_0 \qquad (3)$$

where $x_0 = x(RH = 0)$ is the lattice parameter at RH =0%, and $\delta_0 = x_0 - x(RH = 100)$. The same values of parameter B from Langmuir isotherms above are used.

For further comparison, Figure 5(E) shows the density as a function of the water content. Again, simulation results agree with experiments.

Direct simulations in the osmotic ensemble, as proposed here, have been successfully used to model sorption and hysteresis in phases in a cement system with small volume change under sorption [15]. However, the literature shows that direct simulations in the osmotic ensemble on microporous phases exhibiting large volume changes under sorption generally cannot capture experimental reversibility at high RH (a review of simulations in the osmotic ensemble and associated difficulties can be found in ref. [30]). This observation was reported for various microporous materials such as MOFs (i.e metal-organic frameworks, see [31, 32]). Transition states involving larger volumes changes requires complex transformations in the configurational space, which includes significant changes in atoms coordinates and sorbate amount [31]. Bouquet at al. [31] mention the possible existence of an inherent obstacle to the direct simulation of this

system in the osmotic ensemble to capture the transitions required to describe the full reversibility in system with large volume variations under sorption. In that direction, the existence of a significant energy barrier between metaettringite and ettringite could explain the difficulty of standard GCMC to capture the reversibility. The larger the energy barrier, the harder is to capture by the transition state in a reaction path needed to capture the transition (indeed, according the transition state theory, the rate constant of a transformation process associated with a given free-energy barrier ΔG scales with $exp[-\Delta G/(kT)]$, therefore, large energy barriers demands larger sampling times, which can be prohibitive for GCMC simulations). Other better-suited simulation techniques (e.g. Wang-Landau free energy [31] or using force fields fine-tuned to impose the flexibility of the crystal framework [33]) have been proposed to capture the reversibility at high RH. Therefore, provided the large volume changes associated with ettringite desorption and according to the literature and microporous adsorbing materials, it is expected that the reversibility in the adsorption cycle is not observed in the simulations at high RH as is the case in the experiments

Figure 5: Anisotropic volume changes under desorption:comparison of (A)-(C) lattice parameters (a, b and c) and (D) volume changes obtained from simulations against the experimental data of Baquerizo et al. [3], Zhou et al. [4], and Gard (cited by [4]). (E) Density changes as a function of the water content comparison against Baquerizo et al. [3] and the trend (dashed line) proposed by same authors: $\rho = 2.600 - 0.02925(n+6)$ in g/cm^3 (adapted to the notation used here).

3.2. Coefficient of crystal shrinkage of ettringite

The tensor of crystal shrinkage $\varepsilon^{dry}(RH)$ can be computed from the lattice parameters

obtained from the simulations from Figure 5. According to the hexagonal crystal symmetry of ettringite, $\varepsilon^{sh.}(RH)$ has three independent components in the form:

$$\varepsilon^{dry}(RH) = \begin{pmatrix} \varepsilon_{xx}(RH) & \varepsilon_{xy}(RH) & 0 \\ \varepsilon_{xy}(RH) & \varepsilon_{yy}(RH) & 0 \\ 0 & 0 & \varepsilon_{zz}(RH) \end{pmatrix} \quad (4)$$

where the components $\varepsilon_{xz} = \varepsilon_{yz} = 0$ and (due to the symmetry) $\varepsilon_{xy} = \varepsilon_{yx}$. The hypothesis of infinitesimal strain is not compatible with the large dimension changes in ettringite. Therefore, we adopt the Lagrangian finite strain tensor (which accounts for large strains) to compute the deformations from lattice parameters. In a triclinic system, the Lagrangian deformation tensor ε_{ij} is obtained from the matrices associated with the metric of the reference $h_0 = [a_0, b_0, c_0]_{x,y,z}$ and deformed $h = [a, b, c]_{x,y,z}$ supercell (i.e. the columns of h matrices correpond to the components of the lattice vectors in an orthogonal frame x, y, z):

$$\varepsilon_{ij} = \frac{1}{2}\left[(h_0^{-1})^T h^T h h_0^{-1} - I \right], \quad (5)$$

where I is the identity matrix, and the superscript $[\star]^T$ is a matrix transpose.

The components of the Lagrangian tensor of crystal shrinkage ε^{dry} of ettringite are shown in Figure 6 (A) and (C) as a function of the RH and the water content, respectively. We use the fit of the lattice parameters from Eq. 3 to compute the deformations. In the ettringite domain, the infinitesimal strain hypothesis approximates the results obtained as shown in Figure 6 (B) and (D) as a function of the RH and water content, respectively. The components of the Lagrangian tensor of crystal shrinkage of ettringite are proportional to the water content.

Figure 6: Components of strain tensor obtained from simulations using Eq. 5 as a function of (A)

the RH (with (B) zoom in the small strain domain), and (C) the water content (with (D) zoom in the small strain domain). Linear fitting of the small strain domain are provided for both cases.

3.3. The structure of metaettringite

The agreement of simulations in the desorption branch with the experimental evidence regarding the water content and lattice parameters builds confidence in using our simulation approach to analyze the structural changes associated with metaettringite formation. Figure 7 (A) shows a comparison of X-ray diffraction patterns obtained from experiments and simulation for ettringite at various RH and metaettringite. For comparison, we also show the (experimental) pattern of depujolsite, a mineral that has been associated with metaettringite [4]. We observe that the experimental and simulated patterns in the ettringite domain are consistent, exhibiting the main peak at the same orientations. Most of the peaks in the ettringite pattern disappear in the metaettringite patterns (RH of 0.1 and 0% in the simulated systems), which is in agreement with the experimental data suggesting a more disordered structure for ettringite. Both patterns in the metaettringite domain obtained from simulation are not consistent with the depujolsite structure. Selected snapshots of simulated systems are gathered in Figure 7 (B), in which we observe that the columns, which are very well defined in ettringite, are not well defined in metaettringite structures.

Figure 7: (A) XRD patterns of ettringite and metaettringite according to the RH: comparison of simulation and data from the literature. (B) Selected snapshots of simulated systems show how the columns (indicated by the yellow shadows) in ettringite are not well defined in metaettringite.

To analyze where the main changes occur in ettringite - metaettringite transition, we plot in

the Figure 8 the total pair radial distribution function for systems at RH of 100, 0.1 (desorption) and 0 %. Note that due to the structural similarities as discussed above, the configuration at RH of 100 % can be seen as representative of the ettringite domain. Significant changes in the amplitude of O-H first and second correlation peaks are observed with RH decrease due to the decrease of water content. Other relevant changes in correlation peak amplitudes are observed in S-O and Ca-O pairs.

Figure 8: Total pair radial distribution function $g_{*\_*}(r)$ of ettringite (RH = 100%) and metaettringite (RH = 0.1 and 0%, from desorption branch).

The lack of well-defined peaks in metaettringite XRD patterns and the visual analysis of the snapshots in Figure 7 (B) indicate that metaettringite is a more disordered phase. To quantify the relative order in a molecular system, we use the concept of excess entropy. The pair (first-order) excess entropy S_2 can be computed from the pair radial distribution functions g_{i-j} using [34]:

$$\frac{S_2}{kN} = -\frac{2\pi}{V}\sum_{i,j}\int_0^\infty \left[g_{i-j}(r)\ln g_{i-j}(r) - g_{i-j} + 1 \right] r^2 dr \qquad (6)$$

where N is the total number of particles and x_i is the molecular fraction of particle of type i in the system. Figure 9 shows the total excess entropy S_2 in the desorption branch. The excess entropy is significantly higher in metaettringite when compared to ettringite.

Figure 9: Entropy as function of the RH in the desorption branch: (A) Total and (B) pair-wise entropy. In (C) and (D), we zoom in the low RH domain for (A) and (B), respectively.

3.4. The role of H-bonds on the hysteresis and reversibility

We analyze the number of hydrogen bonds according to the charge balance cation in Fig. 11. We adopt the following criteria to define an H-bonds [35]: donor-acceptor oxygen distance of $2.5 < d_{HB} < 3.5$ Å and angle between O-H and O...O vectors $\theta_{HB} \leq 100^{\circ}$ (see the sketch in Figure 10 indicating how the distance and angle are defined). We separate the contributions to the total H-bonds HB according to the H-bonds between water oxygen HB^{WW}, columns OH groups HB^{CC}, water oxygen and columns OH groups HB^{WC}, sulfate oxygen and water HB^{SW}, and sulfate oxygen and columns OH groups HB^{SC}:

Figure 10: Sketch of a H-bond with indication of the donor-acceptor oxygen distance of d_{HB} and angle between O-H and O...O vectors θ_{HB} used to define the H-bond criteria.

Figure 11: H-bonds as a function of the RH: (A) Total H-bonds HB decomposed in the contributions of H-bonds between (B) sulfate oxygen and water HB^{SW}, (C) sulfate oxygen and columns OH groups HB^{SC}, (D) columns OH groups HB^{CC}, (E) water oxygen and columns OH groups HB^{WC}, and (F) water oxygen HB^{WW}. For H-bonds involving sulfates, the sulfate oxygen function as an acceptor only.

Figure 12: H-bonds as a function of the water content: (A) Total H-bonds HB decomposed in the contributions of H-bonds between (B) sulfate oxygen and water HB^{SW}, (C) sulfate oxygen and columns OH groups HB^{SC}, (D) columns OH groups HB^{CC}, (E) water oxygen and columns OH

groups HB^{WC}, and (F) water oxygen HB^{WW}. For H-bonds involving sulfates, the sulfate oxygen function as an acceptor only.

$$HB = HB^{WW} + HB^{CC} + HB^{WC} + HB^{SW} + HB^{SC} \quad (7)$$

Figures 11 and 12 show the total and pairwise contributions as a function of the RH and the water content, respectively. The conditions associated with Skoblinskaya et al. [28] (Figure 2) isotherms (with rewetting at 30, 1 an d 0.1 % RH) are adopted.

Due to the decrease in water content, the total H-bonds (A) as well as the H-bond involving water ((B), (E), and (F) pairs) decrease with desorption. An increase in (D) HB^{CC} and (C) HB^{SC} with desorption shows that direct interaction between OH groups from neighboring columns and between OH groups and sulfates becomes more significant with drying. These newly formed H-bonds contribute to the cohesion of the dried material, making it difficult for water molecules to ingress in the structure upon rewetting. Indeed, for the adsorption branch with rewetting at an RH of 0.1%, there are HB^{CC} and HB^{SC} remaining even at high RH, which suggest that these H-bonds can be one of the main contributors to hysteresis. In the ettringite domain H-bonds breaking and formation are reversible and follow the same path as desorption as indicated by the curves of adsorption with rewetting at RH of 30 and 1%.

In Figure 12 (A), we observe that the total H-bonds varies linearly with the water content irrespective of the sorption branch considered. In (B), HB^{SW} also displays a linear increasing evolution with the water content. The (C) HB^{SC} and (D) HB^{CC} are a decreasing linear function for $(n+6) > 15$. The (F) HB^{WW} scales as $(n+6)^2$, which is also observed in other microporous materials [14]. These results show that the water content is the variable to be considered in the evaluation of properties of ettringite under sorption instead of the RH (which is associated

ambiguously to the desorption branch and various adsorption branches according to a given rewetting RH).

4. Conclusion

In this work, we performed molecular simulations to understand sorption processes in ettringite from the relevant scale of the adsorption phenomenon (i.e. the molecular scale). Our results provide a fundamental understanding of sorption processes in ettringite that may contribute to new strategies to optimize and conceive new AF-phases rich materials for tailored applications (e.g. thermal energy storage) as well as shed light on the role of ettringite in drying shrinkage of cement-based materials [21]. The main conclusions are:

- Direct simulation in the osmotic ensemble capture the water content and lattice parameters changes in ettringite under desorption, which allows investigating the structural changes that lead to metaettringite formation. The experimental reversibility under sorption in the ettringite domain (i.e. water content in the range $(n+6) = 30\text{-}33$) is also reproduced by the hybrid GCMC-NPT simulations. The large volume variation of ettringite under sorption is captured by the simulations. This variation makes it difficult to direct simulation in the osmotic ensemble to capture the full reversibility in the adsorption process when the rewetting RH is in the metaettringite domain (i.e. water content in the range $(n+6) =$ 11-13).
- The coefficient of crystal shrinkage of ettringite computed using Lagrangian finite strain can be used in multiscale approaches for modeling drying shrinkage in ettringite-rich materials. This is an example of fundamental component data that can be computed using atomistic simulations.

- The structural features of metaettringite with atomic-level detail are analyzed for the first time. We show that metaettringite formation involves $Ca_2Al_6(OH)_{12}$ columns collapse. We have quantified the entropy increase due to a more disordered structure at the metaettringite domain. Sorption-induced stress on the order of hundreds of megapascals is exerted in the columns as the RH decreases. These stresses must play a critical role in columns collapse.
- Upon drying, H-bonds between OH groups from neighboring columns and between OH groups and sulfates are formed, making it difficult to water molecules ingress in the structure upon rewetting. In the ettringite domain, H-bonds breaking and formation are reversible and follow the same path as desorption. Following the discussion in Chen et al. [14], hysteresis under sorption originates from a complex coupling between the fluid grand free energy and the microporous solid energy landscapes. Even if H-bonds are not the origin *per se* of sorption hysteresis, H-bonds are directly related to the fluid grand free energy, being therefore an important ingredient to understand hysteresis under sorption.

Perspectives of this work include further developments to properly capture reversibility in metaettringite-to-ettringite conversion under adsorption and the effects of the temperature under drained and undrained conditions [36]. Also, the various properties of interest for thermo-mechanical modeling of ettringite-rich materials (elastic constants, thermal properties) can be computed for metaettringite using the atomic configurations provided in this study (see supplementary material) and the appropriate simulation protocols.

References

[1] B. Chen, F. Kuznik, M. Horgnies, K. Johannes, V. Morin, E. Gengembre, Physicochemical

properties of ettringite/meta-ettringite for thermal energy storage: Review 193 320–334. doi:10.1016/j.solmat.2018.12.013.
URL http://www.sciencedirect.com/science/article/pii/S0927024818305828

[2] L. J. Struble, P. W. Brown, An evaluation of ettringite and related compounds for use in solar energy storage. doi:10.6028/NBS.IR.84-2942.
URL https://nvlpubs.nist.gov/nistpubs/Legacy/IR/nbsir84-2942.pdf

[3] L. G. Baquerizo, T. Matschei, K. L. Scrivener, Impact of water activity on the stability of ettringite 79 31–44. doi:10.1016/j.cemconres.2015.07.008.
URL http://www.sciencedirect.com/science/article/pii/S0008884615001970

[4] Q. Zhou, E. Lachowski, F. Glasser, Metaettringite, a decomposition product of ettringite 34 (4) 703–710. doi:10.1016/j.cemconres.2003.10.027.

[5] H. Manzano, A. Ayuela, A. Telesca, P. J. M. Monteiro, J. S. Dolado, Ettringite strengthening at high pressures induced by the densification of the hydrogen bond network 116 (30) 16138–16143. doi:10.1021/jp301822e.
URL http://pubs.acs.org/doi/10.1021/jp301822e

[6] E. Scholtzová, D. Tunega, S. Speziale, Mechanical properties of ettringite and thaumasite—DFT and experimental study 77 9–15.

doi:10.1016/j.cemconres.2015.06.008.

URL

http://www.sciencedirect.com/science/article/pii/S0008884615001775

[7] E. Scholtzová, L. Kucková, J. Kožšek, D. Tunega, Structural and spectroscopic characterization of ettringite mineral –combined DFT and experimental study 1100 215–224. doi:10.1016/j.molstruc.2015.06.075.

URL

https://linkinghub.elsevier.com/retrieve/pii/S0022286015301022

[8] L. Liu, A. Jaramillo-Botero, W. A. Goddard, H. Sun, Development of a ReaxFF reactive force field for ettringite and study of its mechanical failure modes from reactive dynamics simulations 116 (15) 3918–3925. doi:10.1021/jp210135j.

URL http://pubs.acs.org/doi/10.1021/jp210135j

[9] T. Honorio, P. Guerra, A. Bourdot, Molecular simulation of the structure and elastic properties of ettringite and monosulfoaluminate 135 106126.

doi:10.1016/j.cemconres.2020.106126.

URL

http://www.sciencedirect.com/science/article/pii/S0008884619306714

[10] W. Sun, D. Wang, L. Wang, Molecular dynamic simulation of failure of ettringite 419 012011. doi:10.1088/1742-6596/419/1/012011.

URL

http://stacks.iop.org/1742-6596/419/i=1/a=012011?key=crossref.446991660526c03931dbb498844696e3

[11] A. G. Kalinichev, R. J. Kirkpatrick, Molecular dynamics modeling of chloride binding to the surfaces of calcium hydroxide, hydrated calcium aluminate, and calcium silicate phases 14 (8) 3539–3549. doi:10.1021/cm0107070.

URL http://dx.doi.org/10.1021/cm0107070

[12] M. Medala, C. Labbez, I. Pochard, A. Nonat, Ettringite surface chemistry: Interplay of electrostatic and ion specificity 354 (2) 765–770.

doi:10.1016/j.jcis.2010.11.031.

URL

http://www.sciencedirect.com/science/article/pii/S0021979710013093

[13] I. Brovchenko, A. Oleinikova, Interfacial and Confined Water, Elsevier.

[14] M. Chen, B. Coasne, R. Guyer, D. Derome, J. Carmeliet, Role of hydrogen bonding in hysteresis observed in sorption-induced swelling of soft nanoporous polymers 9 (1) 3507.

doi:10.1038/s41467-018-05897-9.

URL https://www.nature.com/articles/s41467-018-05897-9

[15] T. Honorio, O. M. Chemgne Tamouya, Z. Shi, A. Bourdot, Intermolecular interactions of nanocrystalline alkali-silica reaction products under sorption 136 106155.

doi:10.1016/j.cemconres.2020.106155.

URL

http://www.sciencedirect.com/science/article/pii/S0008884620302453

[16] A. E. Moore, H. F. W. Taylor, Crystal structure of ettringite 26 (4) 386–393. doi:10.1107/S0567740870002443.
URL //scripts.iucr.org/cgi-bin/paper?a07390

[17] M. Chen, B. Coasne, D. Derome, J. Carmeliet, Coupling of sorption and deformation in soft nanoporous polymers: Molecular simulation and poromechanics 137 103830. doi:10.1016/j.jmps.2019.103830.
URL
http://www.sciencedirect.com/science/article/pii/S0022509619305010

[18] R. T. Cygan, J.-J. Liang, A. G. Kalinichev, Molecular models of hydroxide, oxyhydroxide, and clay phases and the development of a general force field 108 (4) 1255–1266. doi:10.1021/jp0363287.
URL http://dx.doi.org/10.1021/jp0363287

[19] W. R. Cannon, B. M. Pettitt, J. A. McCammon, Sulfate anion in water: Model structural, thermodynamic, and dynamic properties 98 (24) 6225–6230. doi:10.1021/j100075a027.
URL http://pubs.acs.org/doi/abs/10.1021/j100075a027

[20] H. J. C. Berendsen, J. R. Grigera, T. P. Straatsma, The missing term in effective pair potentials 91 (24) 6269–6271. doi:10.1021/j100308a038.
URL http://dx.doi.org/10.1021/j100308a038

[21] M. J. A. Qomi, L. Brochard, T. Honorio, I. Maruyama, M. Vandamme, Advances in atomistic modeling and understanding of drying shrinkage in cementitious materials.

[22] M. Fugel, V. C. Weiss, A corresponding-states analysis of the liquid-vapor equilibrium properties of common water models 146 (6) 064505. doi:10.460 1063/1.4975778.
URL http://aip.scitation.org/doi/10.1063/1.4975778

[23] NIST, SAT-TMMC: Liquid-vapor coexistence properties - SPC/e water, updated November 22, 2016.
URL
http://www.nist.gov/mml/csd/informatics_research/spce_water_sat_lrc.cfm#refs

[24] T. Honorio, Monte carlo molecular modeling of temperature and pressure effects on the interactions between crystalline calcium silicate hydrate layers 35 (11) 3907–3916. doi:10.1021/acs.langmuir.8b04156.
URL https://pubs.acs.org/doi/10.1021/acs.langmuir.8b04156

[25] T. Honorio, L. Brochard, M. Vandamme, Hydration phase diagram of clay particles from molecular simulations 33 (44) 12766–12776. doi:10.1021/acs.langmuir.7b03198.
URL https://doi.org/10.1021/acs.langmuir.7b03198

[26] S. Plimpton, Fast parallel algorithms for short-range molecular dynamics 117 (1) 1–19. doi:10.1006/jcph.1995.1039.

[27] J.-P. Ryckaert, G. Ciccotti, H. J. Berendsen, Numerical integration of the cartesian equations of motion of a system with constraints: molecular dynamics of n-alkanes 23 (3) 327–341. doi:10.1016/0021-9991(77)90098-5.
URL
https://linkinghub.elsevier.com/retrieve/pii/002199917790095

85

[28] N. N. Skoblinskaya, K. G. Krasilnikov, Changes in crystal structure of ettringite on dehydration. 1 5 (4) 381–393. doi:10.1016/0008-8846(75)90093-9.
URL http://www.sciencedirect.com/science/article/pii/0008884675900939

[29] G. Y. Gor, P. Huber, J. Weissmüller, Elastocapillarity in nanopores: Sorption strain from the actions of surface tension and surface stress 2 (8) 086002, publisher: American Physical Society. doi:10.1103/PhysRevMaterials.2.086002.
URL https://link.aps.org/doi/10.1103/PhysRevMaterials.2.086002

[30] F.-X. Coudert, A. Boutin, M. Jeffroy, C. Mellot-Draznieks, A. H. Fuchs, Thermodynamic methods and models to study flexible metal–organic frameworks 12 (2) 247–258, _eprint: https://chemistry-europe.onlinelibrary.wiley.com/doi/pdf/10.1002/cphc.201000590. doi:https://doi.org/10.1002/cphc.201000590.
URL https://chemistry-europe.onlinelibrary.wiley.com/doi/abs/10.1002/cphc.201000590

[31] D. Bousquet, F.-X. Coudert, A. Boutin, Free energy landscapes for the thermodynamic understanding of adsorption-induced deformations and structural transitions in porous materials 137 (4) 044118, publisher: American Institute of Physics. doi:10.1063/1.4738776.
URL https://aip.scitation.org/doi/10.1063/1.4738776

[32] A. Ghoufi, A. Subercaze, Q. Ma, P. Yot, Y. Ke, I. Puente-Orench, T. Devic, V. Guillerm, C. Zhong, C. Serre, G. Férey, G. Maurin, Comparative guest, thermal, and mechanical breathing of the porous metal organic framework MIL-53(cr): A computational exploration supported by experiments 116 (24) 13289–13295. doi:10.1021/jp303686m.
URL https://pubs.acs.org/doi/10.1021/jp303686m

[33] Q. Yang, A. D. Wiersum, H. Jobic, V. Guillerm, C. Serre, P. L. Llewellyn, G. Maurin, Understanding the thermodynamic and kinetic behavior of the CO_2 /CH_4 gas mixture within the porous zirconium terephthalate UiO-66(zr): A joint experimental and modeling approach 115 (28) 13768–13774. doi:10.1021/jp202633t.
URL https://pubs.acs.org/doi/10.1021/jp202633t

[34] A. Baranyai, D. J. Evans, Direct entropy calculation from computer simulation of liquids 40 (7) 3817–3822. doi:10.1103/PhysRevA.40.3817.
URL https://link.aps.org/doi/10.1103/PhysRevA.40.3817

[35] Y. Marcus, Effect of ions on the structure of water: Structure making and breaking 109 (3) 1346–1370. doi:10.1021/cr8003828.
URL http://pubs.acs.org/doi/abs/10.1021/cr8003828

[36] L. Brochard, T. Honório, Revisiting thermo-poro-mechanics under adsorption: Formulation without assuming gibbs-duhem equation 152 103296. doi:10.1016/j.ijengsci.2020.103296.
URL http://www.sciencedirect.com/science/article/pii/S0020722520300847

Authors statement

Tulio Honorio: Conceptualization, Methodology, Investigation, Formal analysis, Writing–original draft, Validation **Maroua Maaroufi**: Investigation, Methodology, Writing–review & editing **Sirine Al Dandachli**: : Investigation **Alexandra Bourdot**: Conceptualization, Writing– review & editing.

Conflict of interest

The authors Tulio Honorio, Maroua Maaroufi, Sirine Al Dandachli, and Alexandra Bourdot of the manuscript “Ettringite hysteresis under sorption from molecular simulations ” submitted to Cement and Concrete Research declare no conflict of interest.

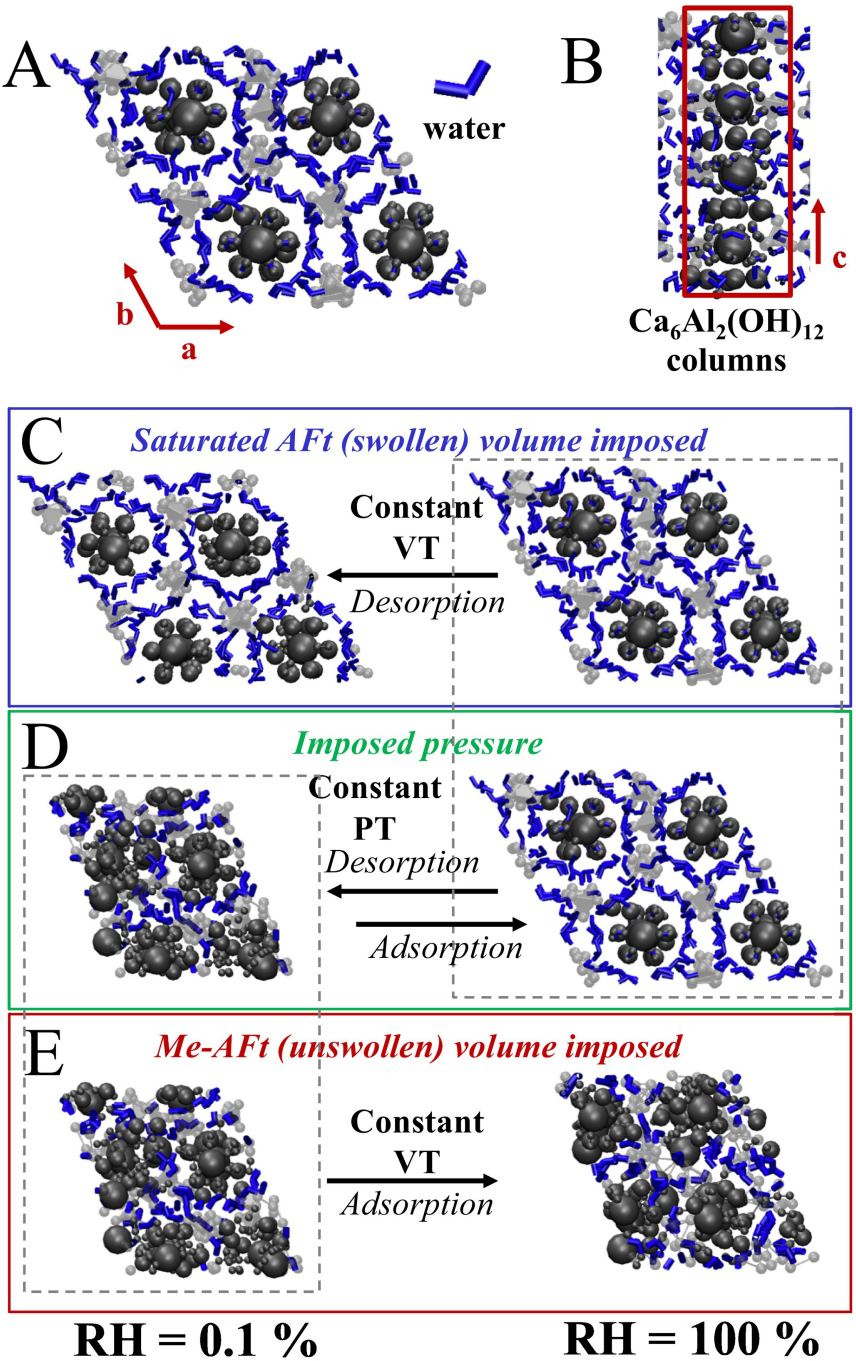
A
water
b
a
B
c
$Ca_6Al_2(OH)_{12}$
columns
C
Saturated AFt (swollen) volume imposed
Constant
VT
Desorption
D
Imposed pressure
Constant
PT
Desorption
Adsorption
E
Me-AFt (unswollen) volume imposed
Constant
VT
Adsorption
RH = 0.1 %
RH = 100 %

Figure 1

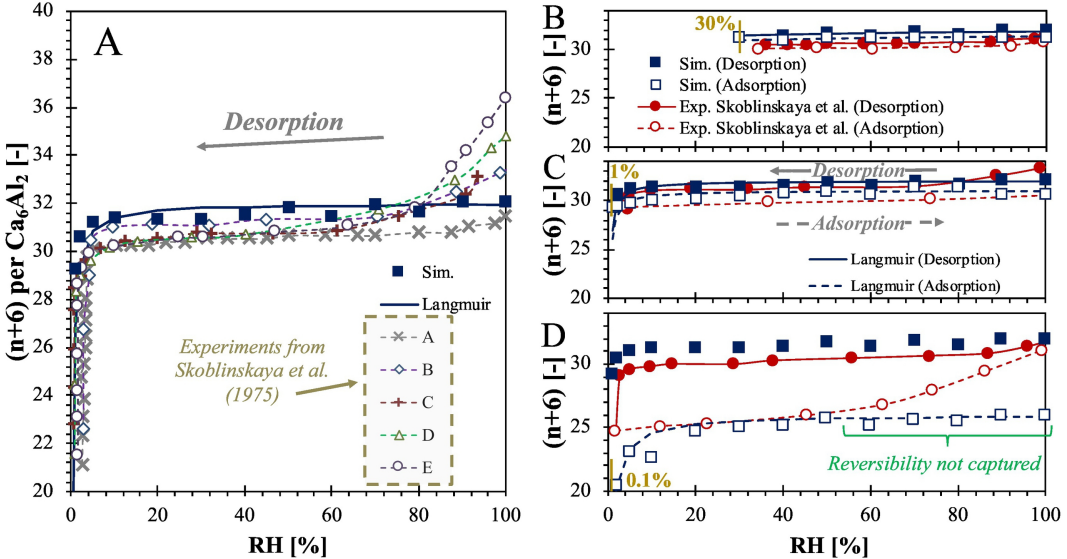
A
Desorption
Sim.
Langmuir
Experiments from Skoblinskaya et al. (1975)
A
B
C
D
E
(n+6) per Ca_6Al_2 [-]
RH [%]
B
30%
Sim. (Desorption)
Sim. (Adsorption)
Exp. Skoblinskaya et al. (Desorption)
Exp. Skoblinskaya et al. (Adsorption)
C
1%
Desorption
Adsorption
Langmuir (Desorption)
Langmuir (Adsorption)
D
0.1%
Reversibility not captured
(n+6) [-]
RH [%]

Figure 2

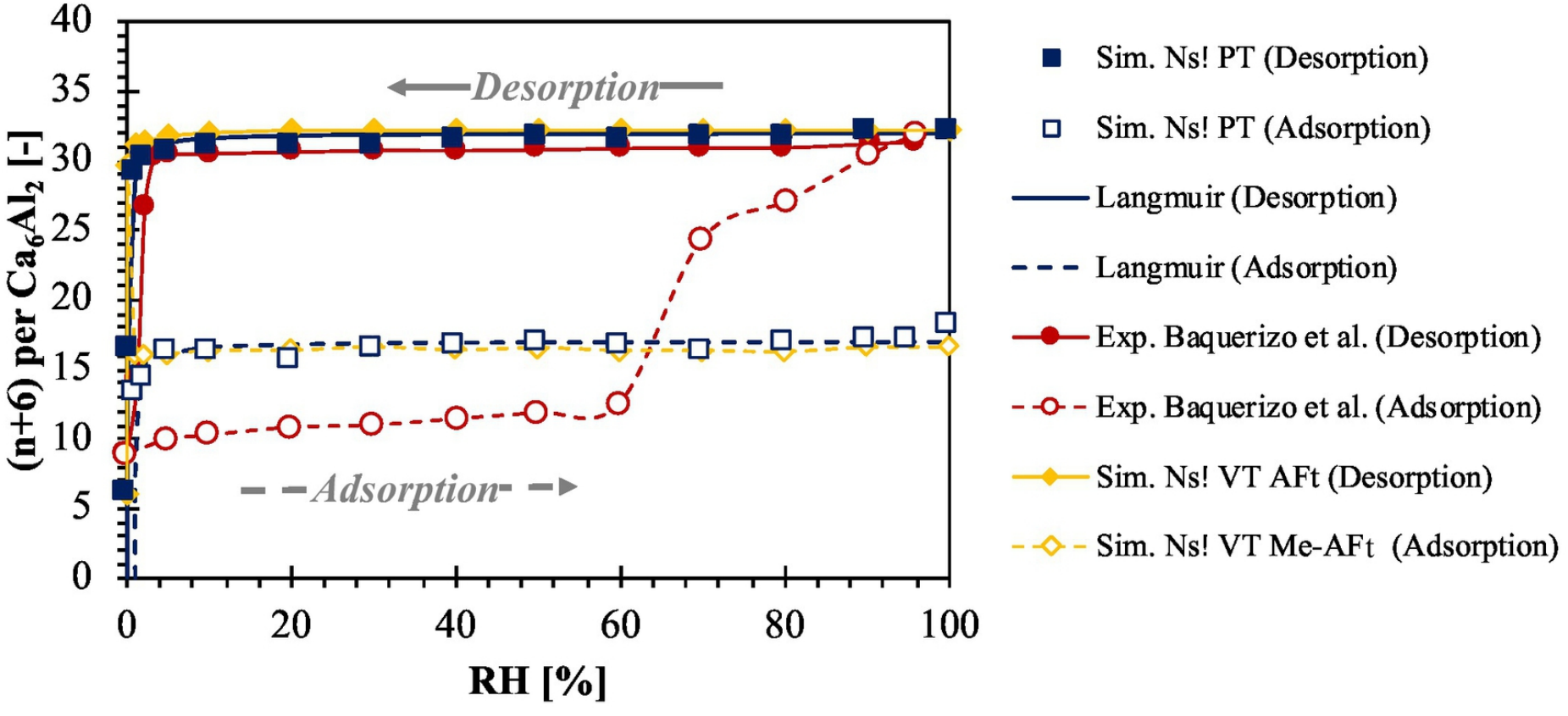
40
35
30
25
20
15
10
5
0
0
20
40
60
80
100
(n+6) per Ca6Al2 [-]
RH [%]
Desorption
Adsorption
Sim. Ns! PT (Desorption)
Sim. Ns! PT (Adsorption)
Langmuir (Desorption)
Langmuir (Adsorption)
Exp. Baquerizo et al. (Desorption)
Exp. Baquerizo et al. (Adsorption)
Sim. Ns! VT AFt (Desorption)
Sim. Ns! VT Me-AFt (Adsorption)

Figure 3

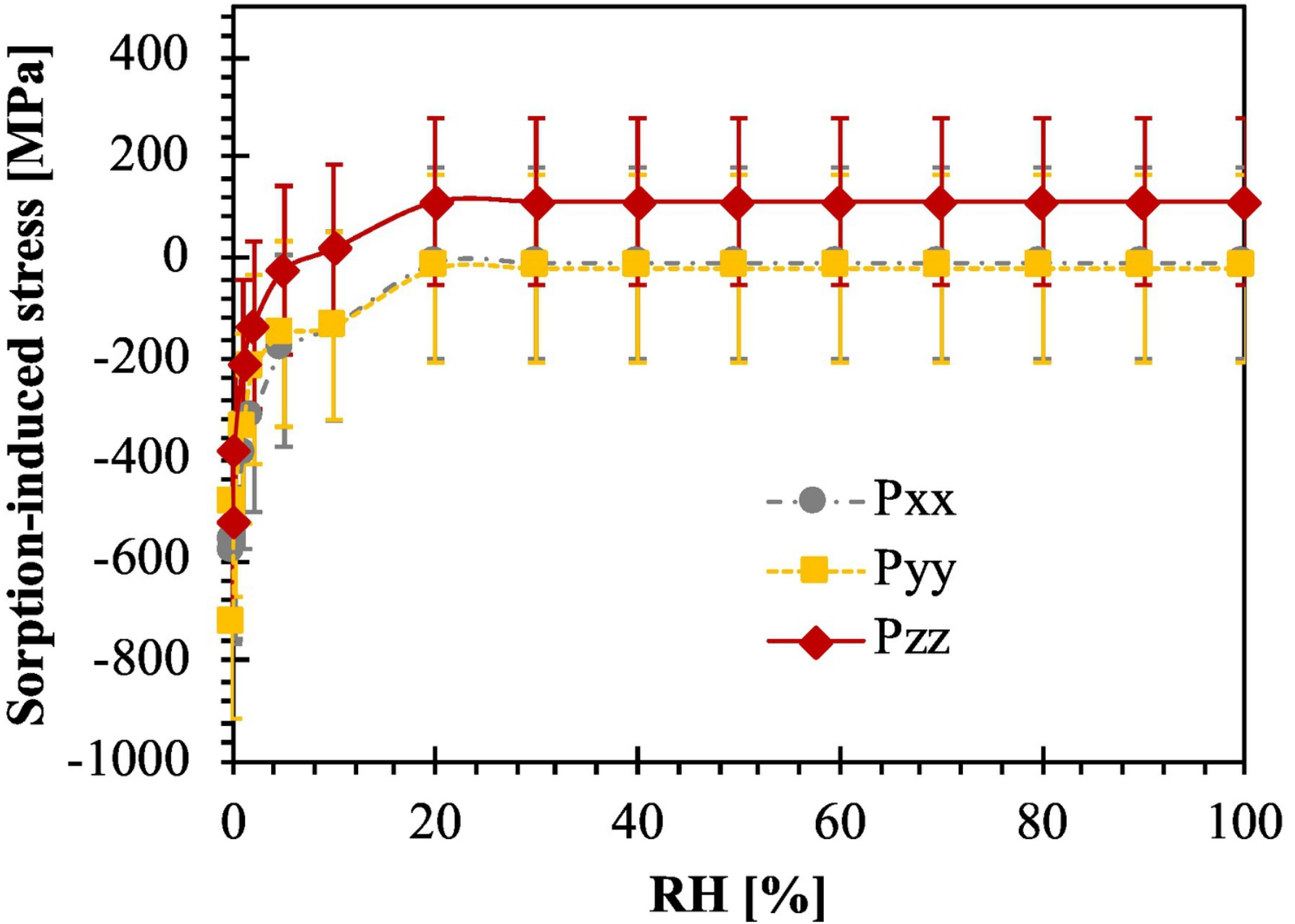
Sorption-induced stress [MPa]
400
200
0
-200
-400
-600
-800
-1000
0
20
40
60
80
100
RH [%]
Pxx
Pyy
Pzz

Figure 4

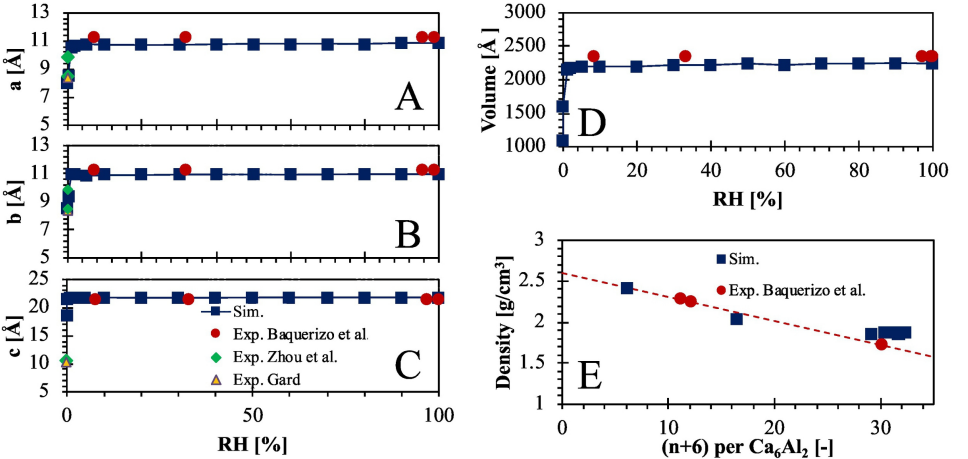
a [Å]
b [Å]
c [Å]
A
B
C
Sim.
Exp. Baquerizo et al.
Exp. Zhou et al.
Exp. Gard
RH [%]
Volume [Å]
D
RH [%]
Density [g/cm³]
Sim.
Exp. Baquerizo et al.
E
(n+6) per Ca6Al2 [-]

Figure 5

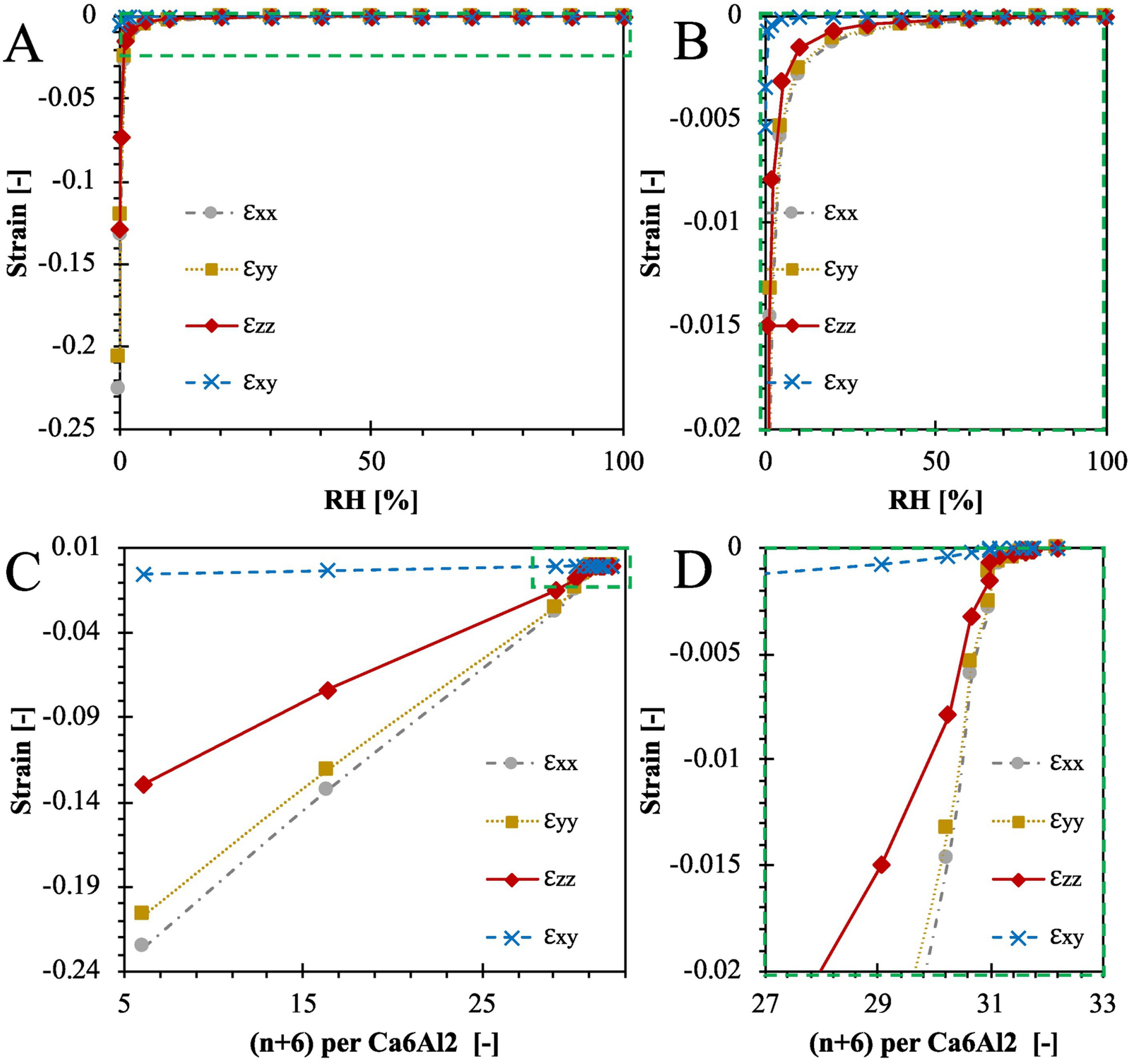
A
B
C
D
Strain [-]
RH [%]
(n+6) per Ca6Al2 [-]
εxx
εyy
εzz
εxy
0
-0.05
-0.1
-0.15
-0.2
-0.25
-0.005
-0.01
-0.015
-0.02
50
100
0.01
-0.04
-0.09
-0.14
-0.19
-0.24
5
15
25
27
29
31
33

Figure 6

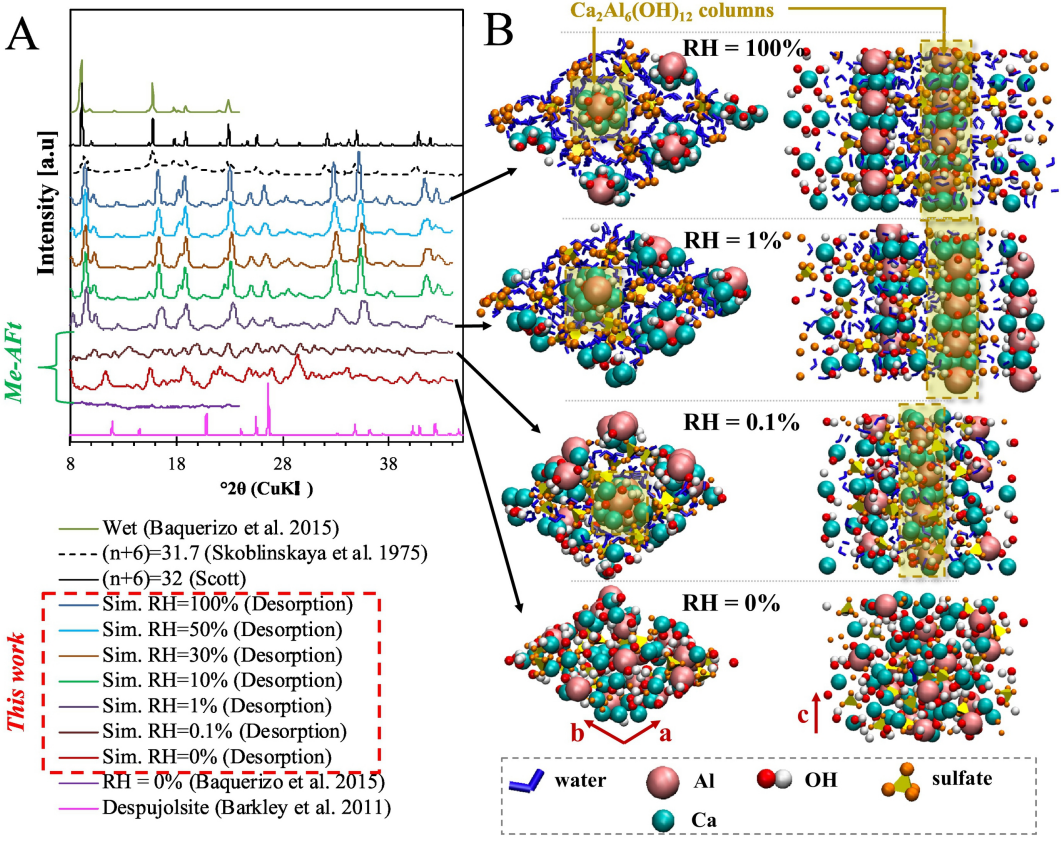
A
Intensity [a.u]
Me-AFt
8
18
28
38
°2θ (CuKI)
Wet (Baquerizo et al. 2015)
(n+6)=31.7 (Skoblinskaya et al. 1975)
(n+6)=32 (Scott)
This work
Sim. RH=100% (Desorption)
Sim. RH=50% (Desorption)
Sim. RH=30% (Desorption)
Sim. RH=10% (Desorption)
Sim. RH=1% (Desorption)
Sim. RH=0.1% (Desorption)
Sim. RH=0% (Desorption)
RH = 0% (Baquerizo et al. 2015)
Despujolsite (Barkley et al. 2011)
B
Ca2Al6(OH)12 columns
RH = 100%
RH = 1%
RH = 0.1%
RH = 0%
b
a
c
water
Al
OH
sulfate
Ca

Figure 7

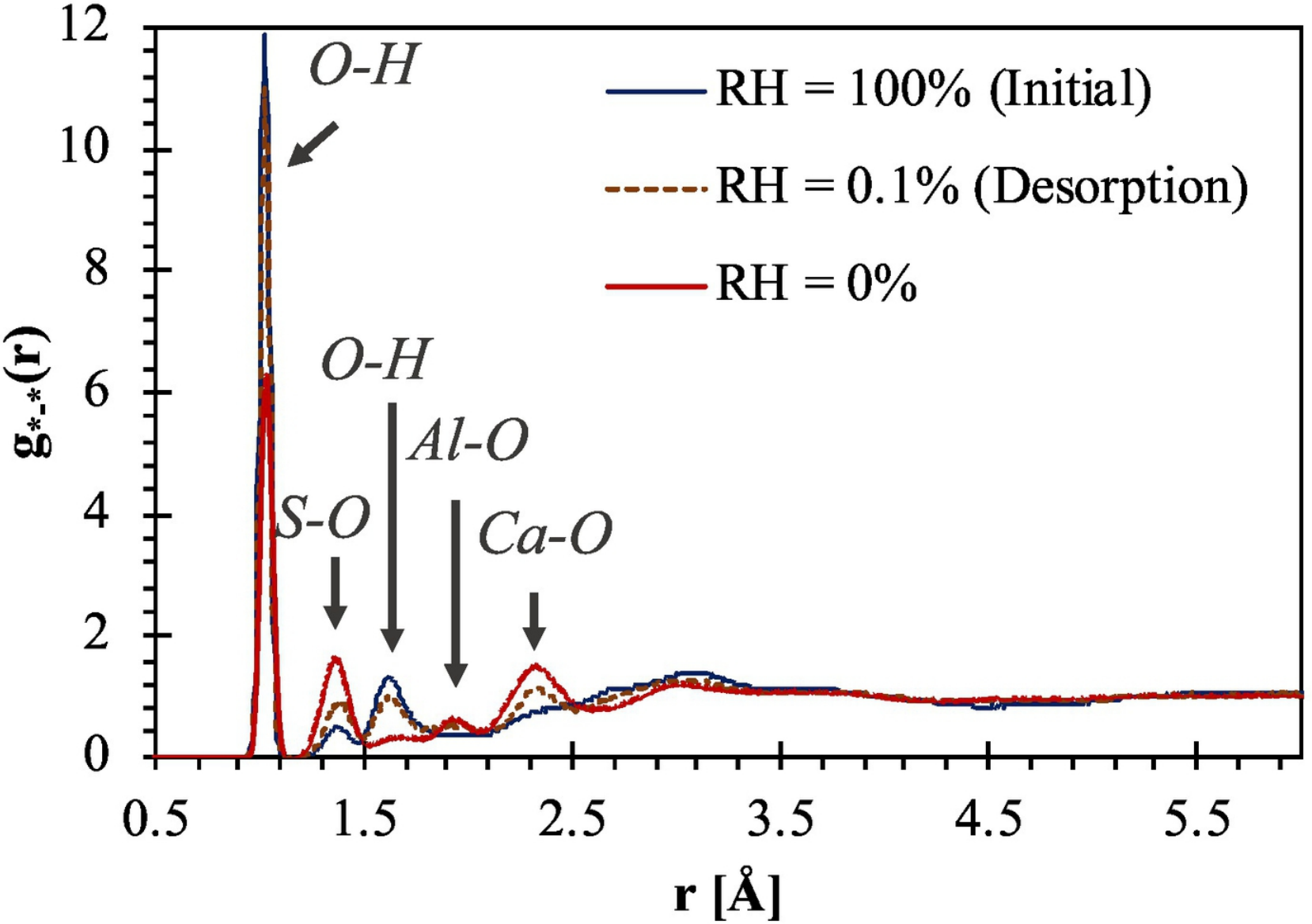
12
10
8
6
4
2
0
g*-*(r)
O-H
O-H
Al-O
S-O
Ca-O
RH = 100% (Initial)
RH = 0.1% (Desorption)
RH = 0%
0.5
1.5
2.5
3.5
4.5
5.5
r [Å]

Figure 8

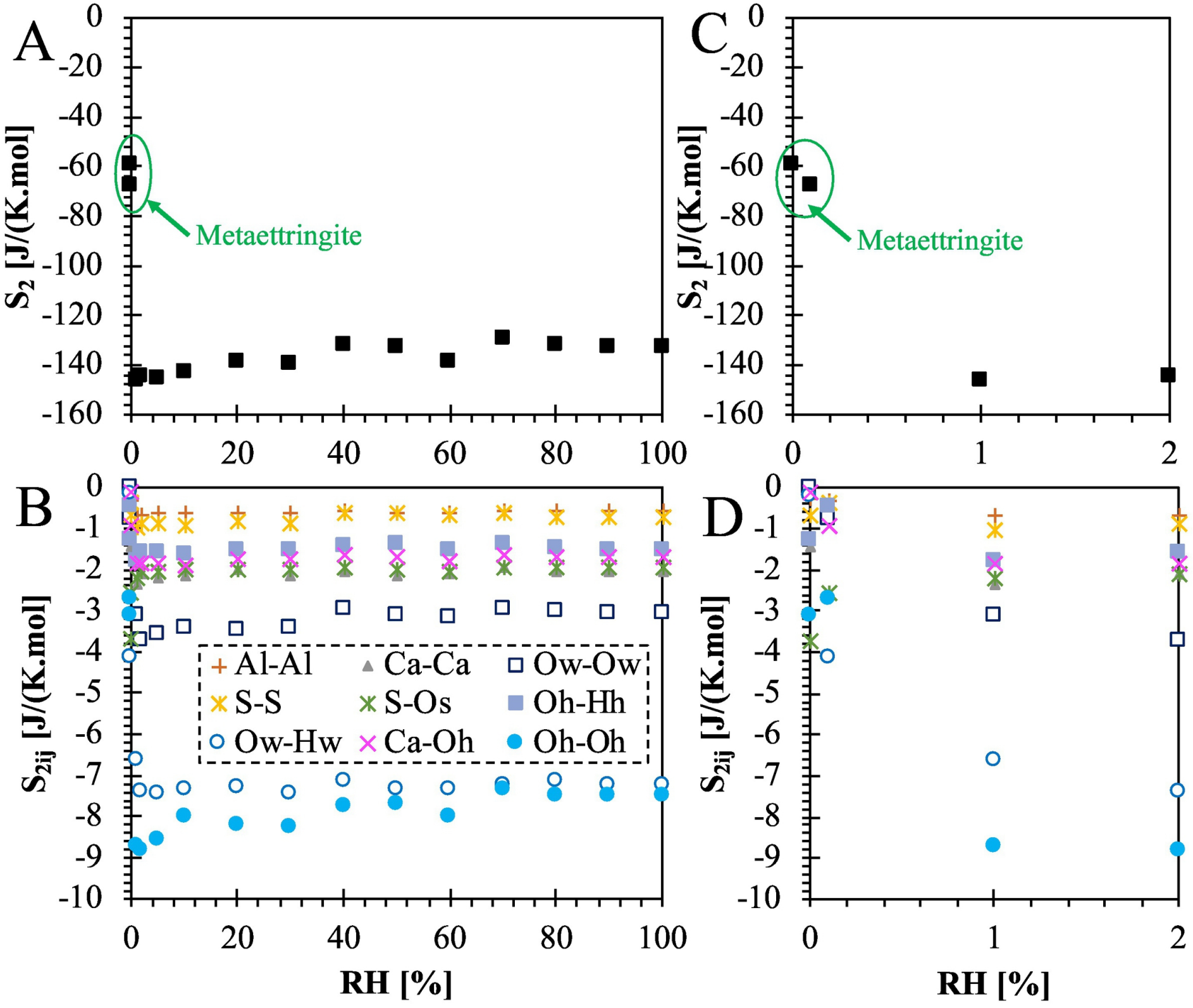
A
C
B
D
Metaettringite
Metaettringite
S_2 [J/(K.mol)]
S_{2ij} [J/(K.mol)]
RH [%]
Al-Al
Ca-Ca
Ow-Ow
S-S
S-Os
Oh-Hh
Ow-Hw
Ca-Oh
Oh-Oh

Figure 9

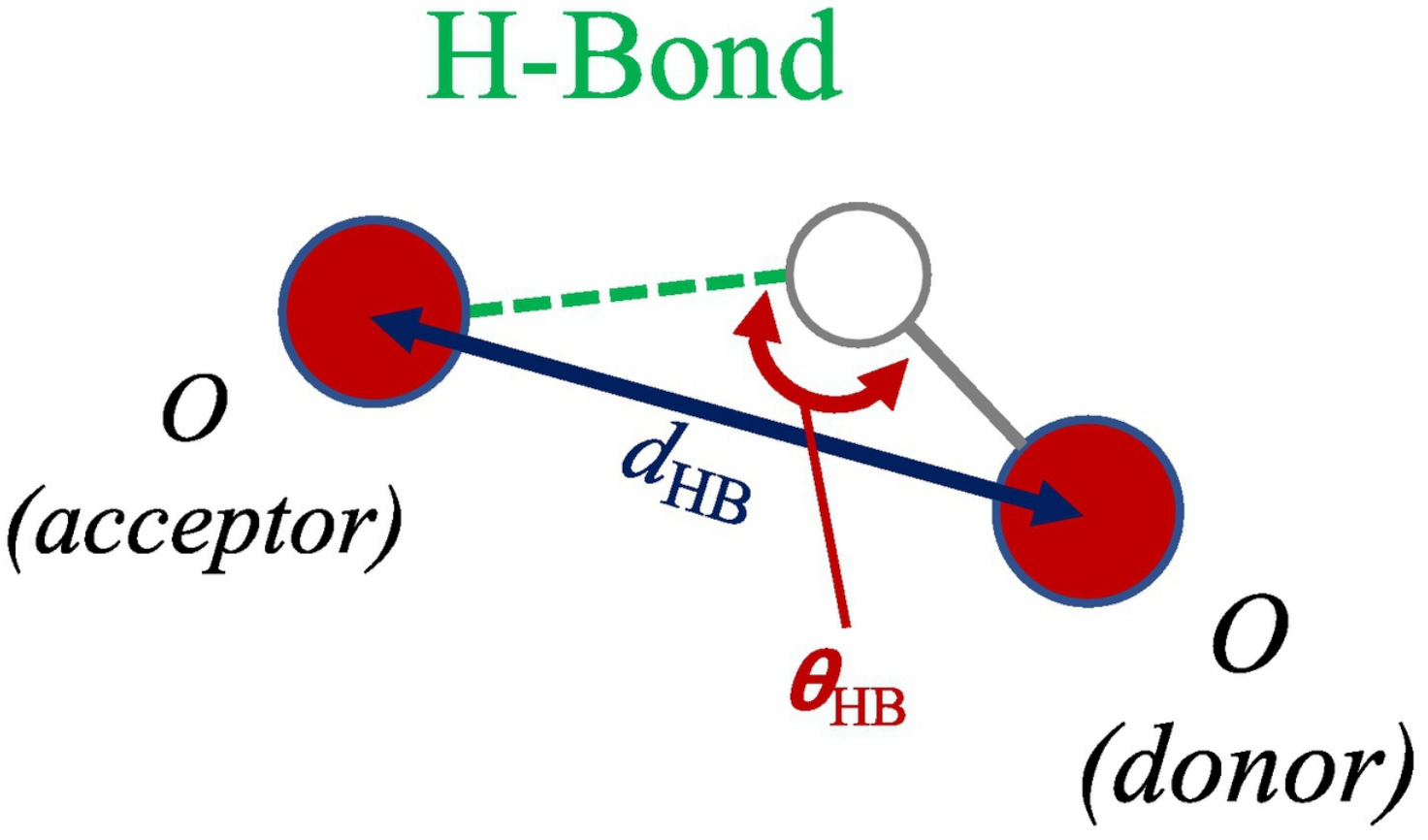

Figure 10

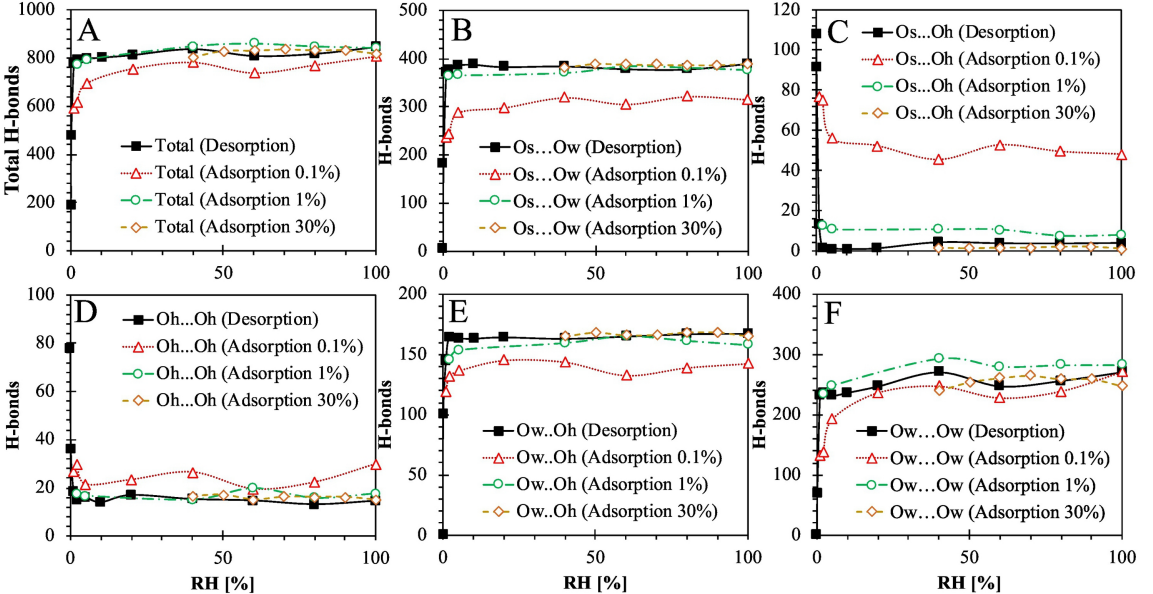
A
Total H-bonds
Total (Desorption)
Total (Adsorption 0.1%)
Total (Adsorption 1%)
Total (Adsorption 30%)
B
H-bonds
Os…Ow (Desorption)
Os…Ow (Adsorption 0.1%)
Os…Ow (Adsorption 1%)
Os…Ow (Adsorption 30%)
C
H-bonds
Os...Oh (Desorption)
Os...Oh (Adsorption 0.1%)
Os...Oh (Adsorption 1%)
Os...Oh (Adsorption 30%)
D
H-bonds
Oh...Oh (Desorption)
Oh...Oh (Adsorption 0.1%)
Oh...Oh (Adsorption 1%)
Oh...Oh (Adsorption 30%)
RH [%]
E
H-bonds
Ow..Oh (Desorption)
Ow..Oh (Adsorption 0.1%)
Ow..Oh (Adsorption 1%)
Ow..Oh (Adsorption 30%)
RH [%]
F
H-bonds
Ow…Ow (Desorption)
Ow…Ow (Adsorption 0.1%)
Ow…Ow (Adsorption 1%)
Ow…Ow (Adsorption 30%)
RH [%]

Figure 11

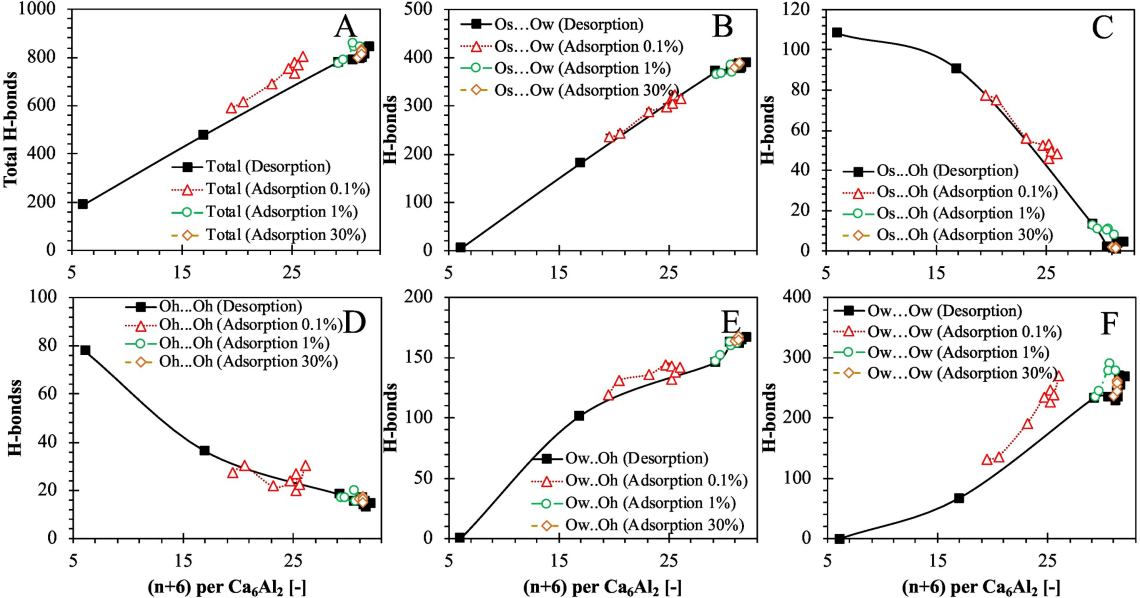
A
Total H-bonds
Total (Desorption)
Total (Adsorption 0.1%)
Total (Adsorption 1%)
Total (Adsorption 30%)
B
H-bonds
Os…Ow (Desorption)
Os…Ow (Adsorption 0.1%)
Os…Ow (Adsorption 1%)
Os…Ow (Adsorption 30%)
C
H-bonds
Os...Oh (Desorption)
Os...Oh (Adsorption 0.1%)
Os...Oh (Adsorption 1%)
Os...Oh (Adsorption 30%)
D
H-bondss
Oh...Oh (Desorption)
Oh...Oh (Adsorption 0.1%)
Oh...Oh (Adsorption 1%)
Oh...Oh (Adsorption 30%)
(n+6) per Ca6Al2 [-]
E
H-bonds
Ow..Oh (Desorption)
Ow..Oh (Adsorption 0.1%)
Ow..Oh (Adsorption 1%)
Ow..Oh (Adsorption 30%)
(n+6) per Ca6Al2 [-]
F
H-bonds
Ow…Ow (Desorption)
Ow…Ow (Adsorption 0.1%)
Ow…Ow (Adsorption 1%)
Ow…Ow (Adsorption 30%)
(n+6) per Ca6Al2 [-]

Figure 12

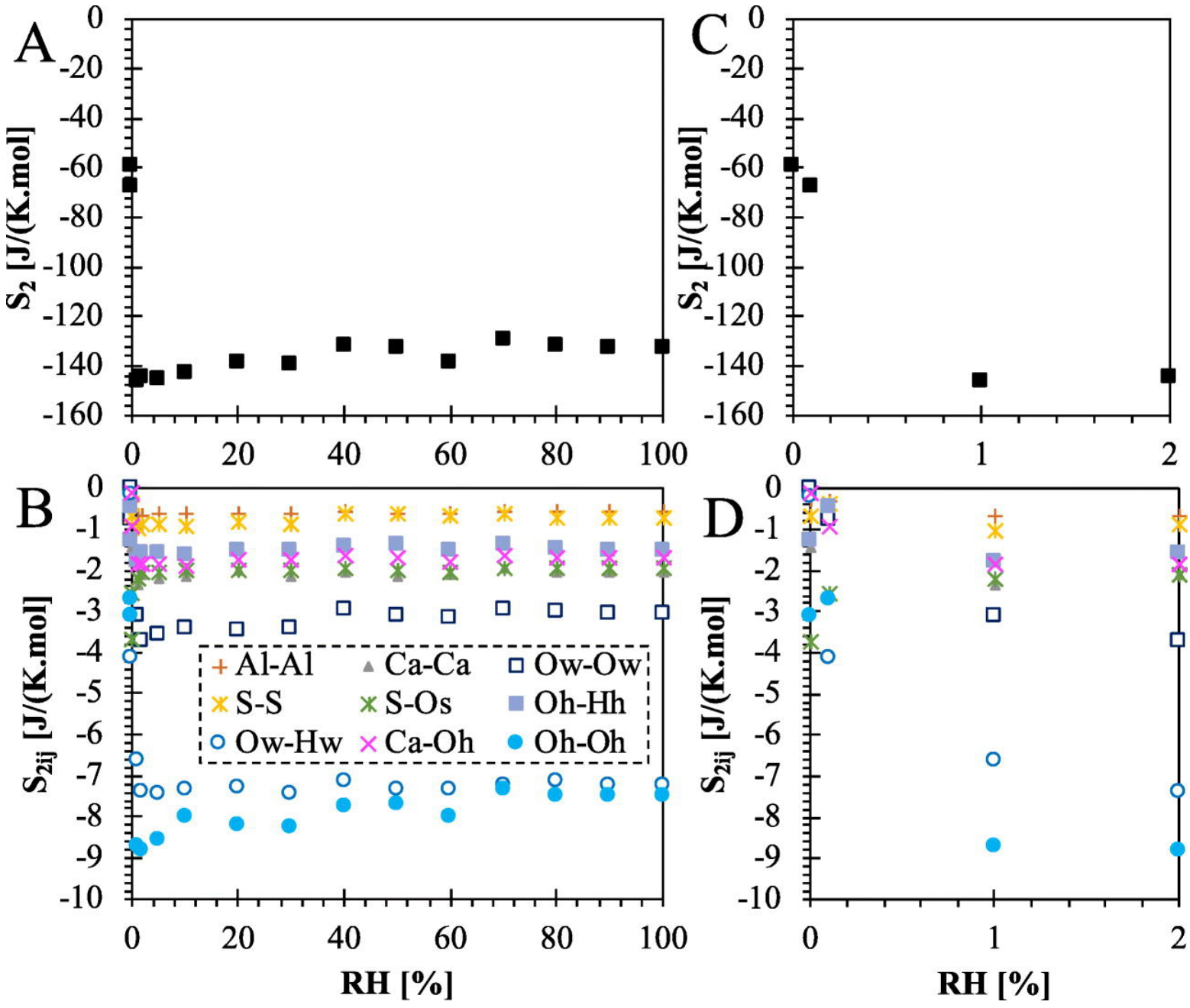

Graphics Abstract